



MnO₂@Co₃O₄ heterostructure composite as high-performance cathode material for rechargeable aqueous zinc-ion battery

Jianhang Sun¹ · Pengchao Zhang¹ · Ying Ba¹ · Juncai Sun¹

Received: 30 November 2022 / Revised: 7 February 2023 / Accepted: 7 March 2023 / Published online: 16 March 2023
© The Author(s), under exclusive licence to Springer-Verlag GmbH Germany, part of Springer Nature 2023

Abstract

In aqueous zinc ion battery, manganese dioxide (MnO₂) has received extensive study as a high-performance cathode material. But the low ionic conductivity and weak diffusion ability prevent its widespread use. In this study, MnO₂@Co₃O₄ composite electrode material is prepared by PVP-assisted hydrothermal method and calcination method. Co₃O₄ nanocrystals (about 5 nm) are fixed on MnO₂ nanorods to form a unique heterostructure, showing an excellent electrochemical performance. The MnO₂@Co₃O₄ composite has a high specific capacity of 350.3 mAh g⁻¹ at 100 mA g⁻¹ and retains 86.2% of its initial capacity after 1200 charge/discharge cycles at 2000 mA g⁻¹. This study offers fresh perspectives on how to build cathode materials with good cycle stability.

Keywords Zinc-ion battery · Nanocomposite cathode · β-MnO₂ nanorods · Heterostructure · High performance

Introduction

Due to the energy crisis caused by the excessive consumption of traditional fossil fuels, there is an increasing demand for clean and renewable energy sources such as solar, wind, and geothermal energy. In recent years, lithium-ion battery is widely applied in digital, technology, and transportation as an energy storage device [1]. Although lithium-ion battery has a high density of energy and a durability, they face challenges such as a scarcity of lithium metal supplies, expensive costs, and inadequate safety [2]. These issues severely restrict its application and further development. Metallic zinc is the suitable anode material for a zinc ion battery since it has a low redox potential, is easily accessible, inexpensive, non-toxic, and safe (−0.76 V vs. normal hydrogen electrode) [3]. It also has outstanding stability in an aqueous solution. Zinc ion battery employing water-electrolyte displays apparent advantages and is extremely ideal for the large power storage system when compared to the fire risk of lithium-ion battery electrolyte. Although ZIBs are expected to have a great future, it is currently very difficult to create

cathode materials with superior electrochemical stability and long service lives.

Currently, organic compounds, Prussian blue analogs, manganese-based materials, and vanadium-based materials make up the majority of the cathode materials used in zinc ion battery. The fact that manganese-based materials have a high theoretical specific capacity of 308 mAh g⁻¹, a high working voltage (from 1.0 to 1.9 V), and a low price make them one of the most attractive candidates for commercial ZIBs [4–6]. However, the polyvalent ions have obvious electrostatic interaction with the cathode material during the cycle, resulting in slow electrochemical kinetics, low capacity and weak rate performance, and the disproportionation reaction of Mn³⁺ leads to the dissolution and collapse of the cathode material [7–9]. Currently, the main strategies to solve the above problems include compounding MnO₂ with carbon materials, introducing defects, doping heteroatoms, and metal ion pre-intercalation. Tang et al. prepared a heterostructure MnS/MnO with double ion defects by electrospinning, and combined it with N-doped carbon fiber to improve the electrochemical activity, reduce the diffusion energy barrier of ions, and obtain excellent rate performance [10]. By using citric acid as complexing agent and weak reducing agent, Zhou et al. prepared K_{0.27}MnO₂·0.54 H₂O pre-embedded with Al³⁺ by one-step hydrothermal method, which improved the stability of the layered structure and accelerated the transfer rate of zinc ions [11]. Long et al. prepared metal ion

✉ Pengchao Zhang
zpc@dlnu.edu.cn

¹ Department of Materials Science and Engineering,
Dalian Maritime University, Dalian 116026,
People's Republic of China

pre-intercalated cathode materials with nano-flower structure, which improved the pseudo-capacitance effect and thus improved the electrochemical performance of the cathode materials [12]. Although the introduction of defects and ion pre-intercalation can significantly improve the electrochemical performance of cathode materials, their complexity, unpredictability, and quantitative difficulty limit the development of commercial applications. Moreover, it is commonly known that the cost of carbon materials is relatively expensive, which restricts its large-scale development.

The current state of lithium-ion battery electrode research indicates that the heterogeneous structure created by metal oxide coating and manganese dioxide can enhance the battery's capacity for storing and cycling stability [13]. The synthesis of heterogeneous electrodes by metal oxide coating is a relatively new technique in the field of ZIBs research, nevertheless. Co_3O_4 nanocrystals can exist stably in weak acidic electrolyte and have excellent catalytic performance. Coupling Co_3O_4 and MnO_2 with differing energy gaps can create a heterogeneous interface that can speed up interfacial reaction kinetics and encourage charge transfer [14]. In this study, we began by making MnO_2 nanorods using an easy hydrothermal process. The MnO_2 nanorods were then suspended under ultrasound with a specific amount of PVP and cobalt nitrate hexahydrate. Manganese dioxide nanorods were exposed to oxidative hydrothermal and calcination processes that resulted in a thin covering of Co_3O_4 . Co_3O_4 coating and MnO_2 nanorods create a heterogeneous structure that may be simultaneously touched by electrolyte without expanding the ion diffusion distance, preventing electrode dissolution and adjusting to structural changes throughout the charge/discharge process [15]. As a result, the composite we created can deliver 350.3 mAh g^{-1} of capacity at 100 mA g^{-1} current density. The composite can achieve a specific capacity of 88.7 mAh g^{-1} at 2000 mA g^{-1} as opposed to the 39.2 mAh g^{-1} of pure- MnO_2 at the same current density. Additionally, the composite retains 86.2% of its initial capacity after 1200 cycles at 2000 mA g^{-1} .

Experimental

Material synthesis

Synthesis of MnO_2 Without additional purification, all substance used in reagents and materials was analytically pure. Typically, deionized water (60 ml) was used to dissolve ammonium persulfate (10 mmol) and manganese sulfate (10 mmol) in turn while stirring. Following transfer, the solution was warmed to $180 \text{ }^\circ\text{C}$ for 12 h in Teflon-lined autoclaves. By centrifuging at 10,000 rpm, cleaning with deionized water, and drying for 12 h at $90 \text{ }^\circ\text{C}$, MnO_2 nanorods were produced.

Synthesis of $\text{MnO}_2@ \text{Co}_3\text{O}_4$ In 40 ml of deionized water, 0.2 g of produced MnO_2 powder was added and ultrasonically mixed for 30 min. A 100-ml hydrothermal reactor was then filled with the mixture after stirring it for 30 min and adding 0.03 g of cobalt nitrate hexahydrate and 0.15 g of PVP. The hydrothermal reactor was maintained at $160 \text{ }^\circ\text{C}$ for 5 h, and then cooled to air temperature while the solid was being collected at 10,000 rpm. The $\text{MnO}_2@ \text{Co}_3\text{O}_4$ powder was created by calcining the obtained solid at $400 \text{ }^\circ\text{C}$ for 3 h at a rate of $2 \text{ }^\circ\text{C min}^{-1}$.

Material characterization

On the Rigaku Ultima IV with Cu $\text{K}\alpha$ radiation, X-ray diffraction (XRD) was applied to analyze the crystal structure of $\text{MnO}_2@ \text{Co}_3\text{O}_4$. To analyze the morphology of the materials, high-resolution transmission electron microscopy (HRTEM) and field emission scanning electron microscopy (FESEM) were also employed. The element distribution of the sample was measured by an energy dispersive X-ray spectrometer (EDS) attached to a scanning electron microscope, and the EDX energy spectrum and the atomic ratio of each element were obtained. Data on the materials' valence states and surface chemical composition were characterized using X-ray photoelectron spectroscopy (XPS).

Electrochemical measurements

Using a CR2032 coin battery, the electrochemical performance of $\text{MnO}_2@ \text{Co}_3\text{O}_4$ was assessed. The electrode is made of $\text{MnO}_2@ \text{Co}_3\text{O}_4$, carbon black (AB), polyvinylidene fluoride (PVDF), and an appropriate amount of *N*-methyl pyrrolidone as the solvent in a mass ratio of 7:2:1. A stainless steel mesh with a 10-mm diameter is covered with the electrode. The electrolyte was an aqueous mixture of 3 M ZnSO_4 and 0.1 M MnSO_4 . At various current densities, the constant current charge and discharge of Zn/Zn^{2+} were measured (potential range from 0.8 V to 1.9 V). A CHI660E electrochemical workstation was used to perform electrochemical impedance spectroscopy (EIS) with a frequency range of 10^{-2} to 10^{-5} Hz and a variety of cyclic voltammetry (CV) curve tests of 0.8–1.9 V (vs. Zn/Zn^{2+}) with different scanning speeds between 0.2 mV s^{-1} and 2.0 mV s^{-1} . All electrochemical tests were performed at room temperature of $26 \text{ }^\circ\text{C}$.

Results and discussion

$\text{MnO}_2@ \text{Co}_3\text{O}_4$ powder preparation is shown in Fig. 1. After ultrasonic stirring, the obtained MnO_2 powder was combined with cobalt nitrate hexahydrate, PVP, and deionized water. After that, a Teflon-lined autoclave was used to seal the suspension and heat it to $160 \text{ }^\circ\text{C}$ for 5 h.

PVP as a surfactant can promote the dispersion of MnO₂ nanorods and provide coordination sites for Co²⁺ as complexing agents [16]. Cobalt ions (Co²⁺) were combined with hydroxyl (–OH) on the surface of manganese dioxide nanorods by electrostatic attraction. After removing the carbon by oxidative calcination at 400 °C in air, MnO₂@Co₃O₄ nanorods were finally produced.

As presented in Fig. 2a, the crystal structure of the MnO₂@Co₃O₄ is investigated by XRD. The diffraction peaks of MnO₂ and β-MnO₂ (JCPDS 24–0735) are perfectly matched. The (220), (311), (400), and (440) reflections of Co₃O₄ (JCPDS 43–1003) are responsible for the diffraction peaks at 31.3°, 36.8°, 44.8°, and 65.2°. A good crystallinity

of the composite is shown by the small and strong diffraction peak of the MnO₂@Co₃O₄. The diffraction peak intensity of Co₃O₄ nanocrystals is weak due to the small content. The produced MnO₂@Co₃O₄ composites were analyzed by XPS to assess their chemical make-up and valence state. The chemical composition and valence states of the MnO₂@Co₃O₄ composite, in which Mn, Co, O, and C elements are discovered, are characterized by the total spectrogram shown in Fig. 2b. The high-resolution Mn 2p spectra (Fig. 2c) show that the composite material has two Mn peaks at 641.8 eV and 653.6 eV. The spin separation energy of Mn 2p^{3/2} and Mn 2p^{1/2} can be calculated to be 11.8 eV. We can prove that the composite contains Mn in the form of β-MnO₂ by

Fig. 1 The preparation diagram of MnO₂@Co₃O₄ heterostructure composites

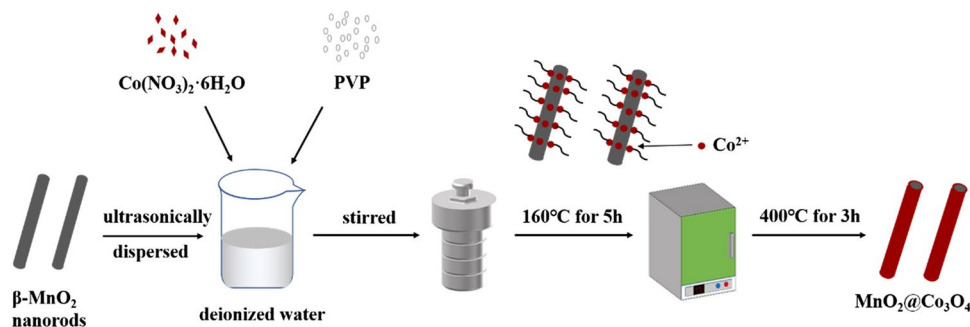
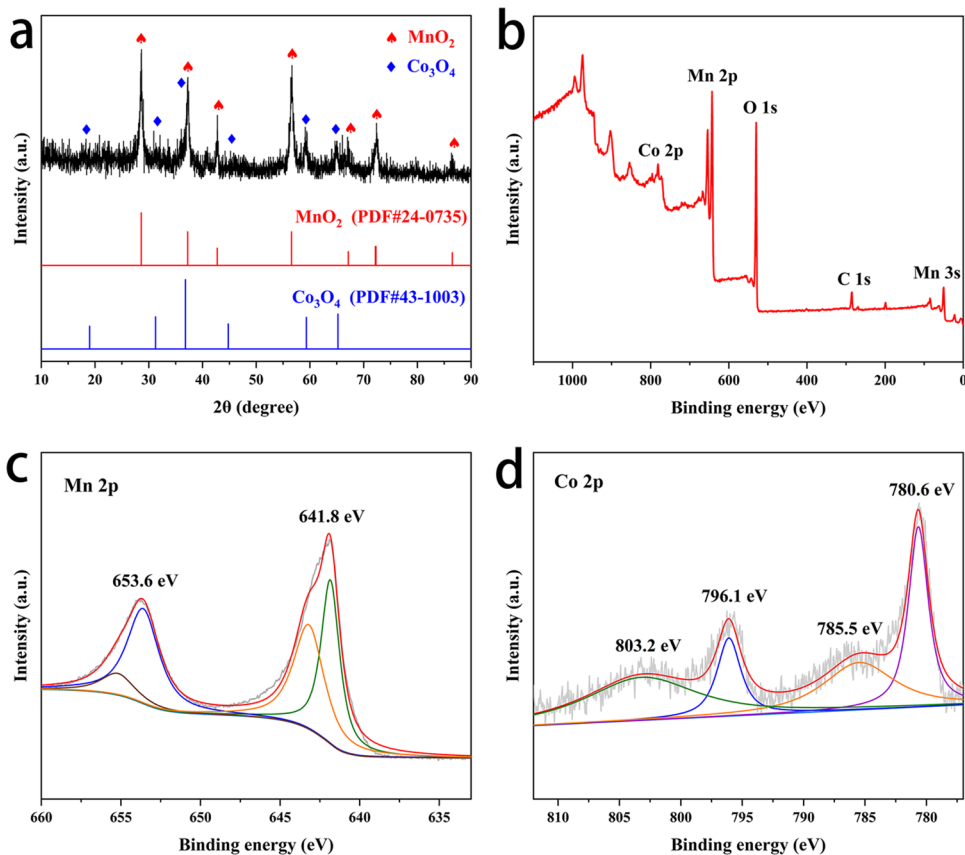


Fig. 2 **a** XRD patterns of MnO₂@Co₃O₄, **b** XPS spectrum of MnO₂@Co₃O₄, **c** high-resolution XPS spectra of MnO₂@Co₃O₄ for Mn 2p and **d** Co 2p



combining the XRD results. The spin separation energy in Fig. 2d is 15.5 eV, and the two pairs of peaks at 780.6 eV and 796.1 eV, respectively, correspond to Co $2p^{3/2}$ and Co $2p^{1/2}$. Co³⁺ is responsible for the fitting peak at 780.6 eV and 796.1 eV, while Co²⁺ is responsible for the two higher peaks at 785.5 eV and 803.2 eV [17]. This result demonstrates the synthesis of Co₃O₄. The binding energy of Mn and Co in the MnO₂@Co₃O₄ combination is somewhat different from that of MnO₂ and Co₃O₄, which is consistent with the previously reported heterogeneous materials. This difference results from the differing electron attraction between Mn and Co [18].

We investigate the samples' microstructure using SEM, as seen in Fig. S1. MnO₂ nanorods have a smooth surface and a diameter of 50–200 nm. The composite still has its original nanorods as seen in Fig. 3a, which is a TEM image of MnO₂@Co₃O₄. Co₃O₄ nanocrystals are evenly coated and directionally generated on the outside of MnO₂ nanorods. The lattice fringe distance of MnO₂ nanorods, which relates to the (110) crystal plane of β -MnO₂ (JCPDS 24–0735), is 0.31 nm, as shown by the HRTEM image in Fig. 3b. Co₃O₄ nanocrystals with a thickness of around 5 nm have been seen covering the surface of MnO₂ nanorods. The (220) crystal plane of Co₃O₄ (JCPDS 43–1003) is responsible for the lattice fringe distance, which is 0.28 nm. The SAED image (Fig. 3c) also displays the diffraction spots of the (110), (002), (400), and (422) planes (Table S1). The results show the coexistence of Co₃O₄ and MnO₂, revealing the composite attribute of polycrystalline MnO₂@Co₃O₄. The elemental mapping Fig. 3d shows that the Mn, Co, and O elements are uniformly distributed in the nanorods. Figure 3e shows the EDX energy spectrum of MnO₂@Co₃O₄, from which

signal peaks of Co, Mn, and O can be detected. Based on the average of three EDX test results, MnO₂@Co₃O₄ can be obtained. The atomic ratio of Co to Mn on the surface is 0.09. Nanorods with heterogeneous structures are formed by the close interaction of Co₃O₄ nanocrystals with MnO₂ nanorods. This contact accelerates ion/electron transfer and improves electron conductivity and provides stability for the initial activation phase of the electrode [19].

To test the electrochemical performance of the MnO₂@Co₃O₄ composite as the cathode material in a water-based zinc ion battery, the produced MnO₂@Co₃O₄ electrode and metal zinc were employed as the cathode and anode materials, respectively. A voltage window of 0.8–1.9 V (vs. Zn²⁺/Zn) was used for all measurements. As seen in Fig. 4a, both the MnO₂ and MnO₂@Co₃O₄ electrodes exhibit electrode activation processes at 0.1 A g⁻¹, which is attributed to the transformation of the tunnel structure of manganese dioxide into a layered structure in the first ten cycles, and the reactive sites of layered phase Zn-buserite (B-Zn_xMnO₂·nH₂O) gradually increase [20]. The MnO₂@Co₃O₄ electrode reached a high specific capacity of 350.1 mAh g⁻¹ after the initial activation process and the capacity is still 327.1 mAh g⁻¹ after 50 cycles with a maintenance rate of 93.4%. In contrast, the MnO₂ electrode showed a significant attenuation trend. In Fig. 4b, the galvanostatic charge/discharge (GCD) curves at 0.1 A g⁻¹ for the MnO₂ electrode and the MnO₂@Co₃O₄ electrode are displayed. The MnO₂@Co₃O₄ electrode has a clearly greater average discharge voltage and discharge platform than the MnO₂ electrode. In the meanwhile, at various current densities, we compare the rate performance of the MnO₂ electrode with the MnO₂@Co₃O₄ electrode. According to Fig. 4c, the reversible capacities of MnO₂@Co₃O₄

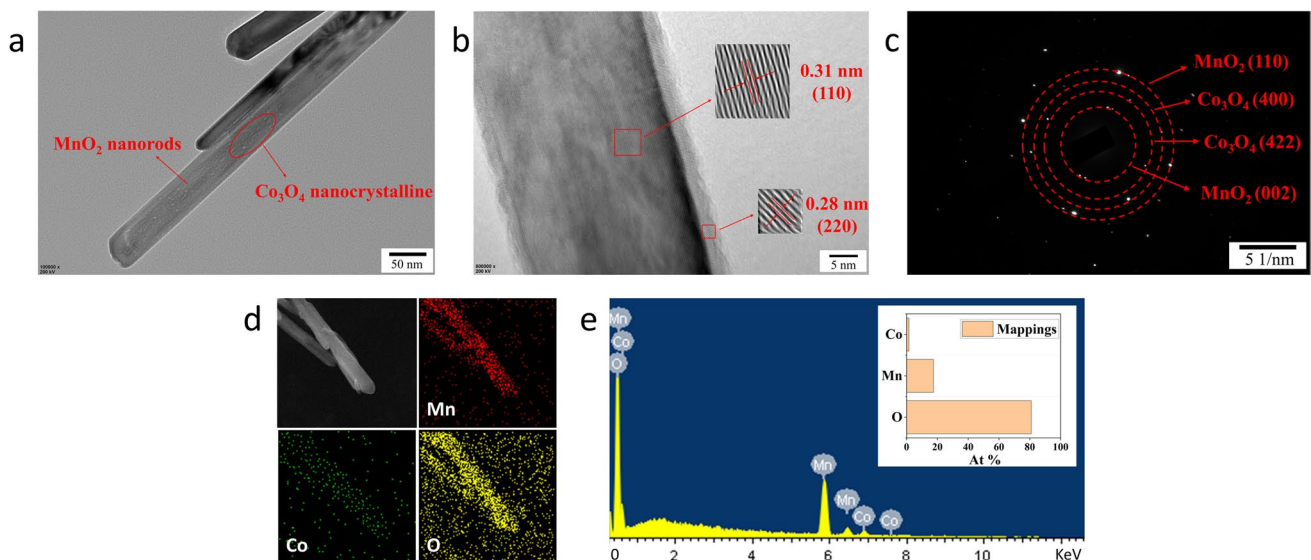


Fig. 3 **a** TEM image of MnO₂@Co₃O₄, **b** HRTEM images of MnO₂@Co₃O₄, **c** SAED image of MnO₂@Co₃O₄ composite, **d** EDS mapping of MnO₂@Co₃O₄, **e** EDX image of MnO₂@Co₃O₄ (The illustration is the corresponding atomic percentage content of Co, Mn, and O)

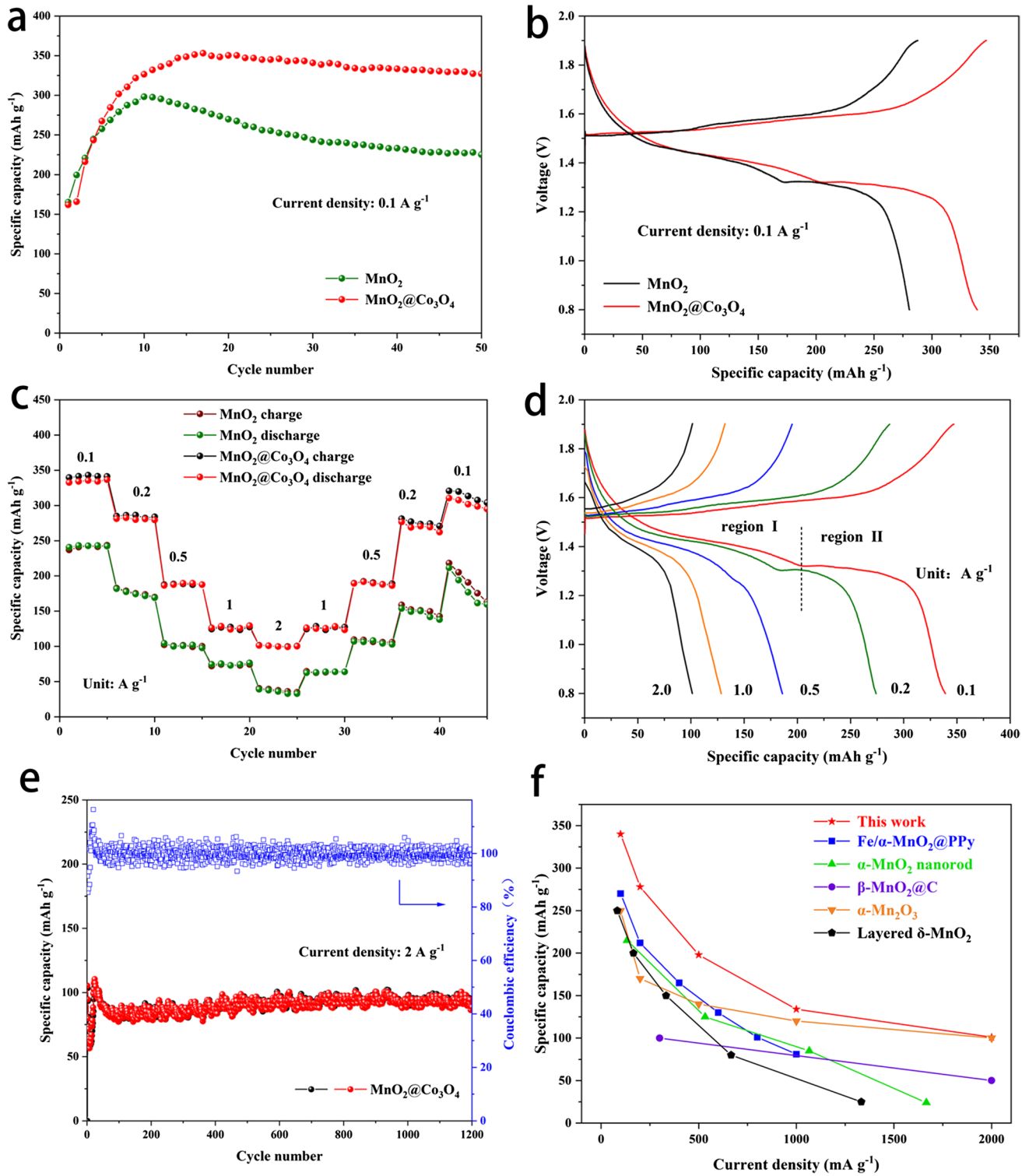


Fig. 4 **a** MnO₂ and MnO₂@Co₃O₄ electrode cycling performance at 0.1 A g⁻¹, **b** MnO₂ and MnO₂@Co₃O₄ electrode galvanostatic charge/discharge (GCD) curves at 0.1 A g⁻¹, **c** rate performance, **d** the MnO₂@Co₃O₄ electrode’s charge/discharge profiles at varied cur-

rent densities, **e** long-term cycling performance of the MnO₂@Co₃O₄ electrode at 2 A g⁻¹, **f** the comparison of the several previously reported cathode materials’ specific capacities

electrodes are 343, 287, 190, 130, and 101 mAh g⁻¹, respectively, for 0.1, 0.2, 0.5, 1.0, and 2.0 A g⁻¹, which are much greater than those of MnO₂ electrode. Due to its great structural stability and high reaction reversibility, the MnO₂@Co₃O₄ electrode has a comparatively high corresponding capacity when the current density is reduced from 2.0 to 0.1 A g⁻¹ [19]. On the other hand, the MnO₂ electrode performs poorly in terms of rate and capacity throughout a range of current densities. For the MnO₂@Co₃O₄ electrode at varied current densities, Fig. 4d shows typical GCD curves. This data was gathered during the preceding cycle of each current density. Under low current density, it can be seen that there is a clear inflection point about 1.3 V. As the current density increases, the contribution of the second discharge platform (region II) to the capacity gradually decreases, and the inflection point disappears when the current density reaches 1 A g⁻¹. The insertion of H⁺ is thought to be responsible for region I's voltage stability, while the insertion of Zn²⁺ is mostly to blame for region II's voltage and capacity decline [21]. Compared with region II, region I has a higher rate of reaction kinetics, which may be related to the various insertion mechanisms used by H⁺ and Zn²⁺. The region I reaction's contribution to the total capacity becomes predominate at high rates as current density rises, and the GCD curves' inflection point gradually vanishes. This should be attributed to the dominant contribution of surface capacitance induction to capacity during high-rate discharge [22].

Figure 4e investigates the long-term cycling stability of the MnO₂@Co₃O₄ electrode at a current density of 2 A g⁻¹. In particular, we found that during long cycles, the capacity stability of the MnO₂ electrode decreased significantly after a short activation process and only maintained at about 36.5 mAh g⁻¹ after 1200 cycles (Fig. S2). Manganese dioxide expansion and stripping resulted in manganese dissolution and loss of active sites, which may be the reason for the capacity reduction [20]. However, after activating the active sites, the MnO₂@Co₃O₄ electrode can achieve the maximum specific capacity of 110.4 mAh g⁻¹, and the capacity retention rate reaches 86.2% after 1200 cycles, as shown in Fig. 4e. The improved electrode cycling performance was attributed to the nanocrystalline coating alleviating the stress effect caused by the phase transition during the initial cycling process and preventing direct contact between manganese dioxide and electrolyte. Meanwhile, the synergistic interaction between the components promotes the rapid diffusion of ionic electrons and enhances the reaction kinetics [19]. In addition, Fig. 4f shows how the rate performance of the MnO₂@Co₃O₄ electrode compares to that of other cathode materials for water-based rechargeable batteries that have been previously described. In comparison

to other aqueous solution ZIB cathode materials, such as Fe/α-MnO₂@PPy [23], α-MnO₂ nanorod [24], β-MnO₂@C [25], α-Mn₂O₃ [26], and layered δ-MnO₂ [27], we created MnO₂@Co₃O₄ electrode with a greater rate capability. According to the above electrochemical characteristics, the MnO₂@Co₃O₄ electrode has a large reversible capacity, great rate performance, and strong cycle stability.

To further research the cause of the improvement in electrochemical performance, we investigated electrochemical kinetics. The electrochemical performance of the created MnO₂@Co₃O₄ electrode was assessed using cyclic voltammetry (CV) with a test voltage range of 0.8–1.9 V and varied scanning speeds of 0.2–2.0 mV s⁻¹. The shape of the CV curve largely stays the same as the scanning rate increases, and there are two sets of distinct redox peaks. The low potential cathode peak is caused by Zn²⁺ insertion into the MnO₂ structure, which reduces Mn⁴⁺ to Mn³⁺. The two oxidation peaks at high potential, which appear simultaneously, are caused by the extraction of Zn²⁺ from the MnO₂ structure, which converts Mn³⁺ to Mn⁴⁺ [28]. At a scanning rate of 0.1 mV s⁻¹, the CV curves of MnO₂ and MnO₂@Co₃O₄ were contrasted in Fig. S3. The MnO₂@Co₃O₄ electrode demonstrated stronger electrochemical reaction activity as evidenced by the fact that its peak response current was much higher than that of the MnO₂ electrode. To further research the dynamics of ion transport, we analyzed CV data at varied scan rates by the following formula [29]

$$i = av^b \quad (1)$$

In most cases, i represents the scan current density (mA), v represents the scanning rate (mV s⁻¹), and a and b values represent the relevant adjustable parameters. The fitting slope of the log i vs log v graph can be calculated to determine the b value, according to the following common formula

$$\log i = \log a + b \log v \quad (2)$$

When the b value is close to 0.5, the capacitance is controlled by ion diffusion. When the b value is close to 1.0, the capacitance process controls it. When the b value is between 0.5 and 1.0, both ion diffusion and capacitance behavior have an impact on capacitance [30]. The values of b are computed to be 0.61, 0.69, 0.70, and 0.50, as illustrated in Fig. 5b. It is clear from this result that a diffusion process mostly controls the charge–discharge process of MnO₂@Co₃O₄. Moreover, the current (i) is divided into capacitance reaction (k_1v) and diffusion reaction ($k_2v^{1/2}$). The contribution rates of capacitance can be calculated by the following formula [31]:

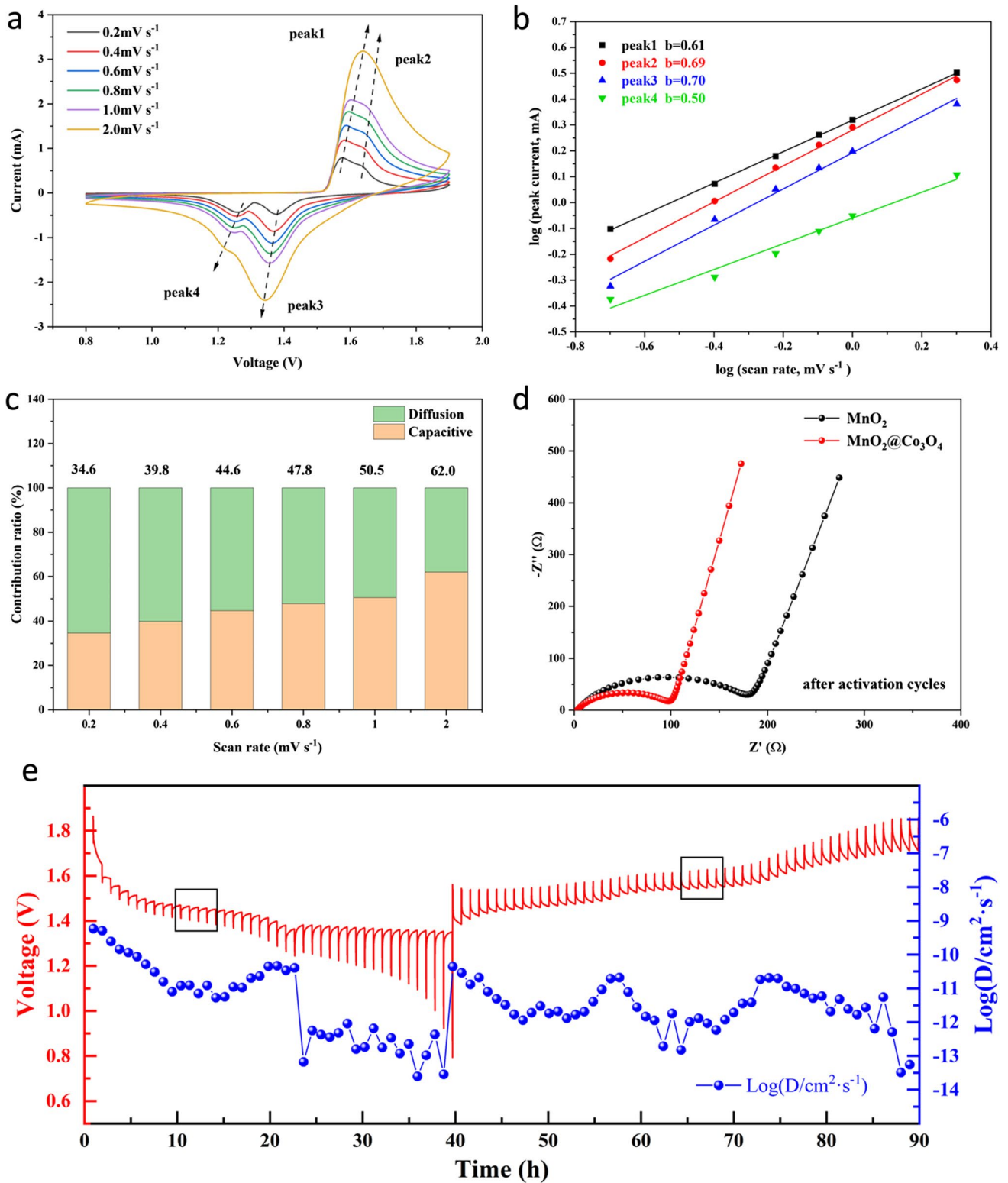


Fig. 5 **a** $\text{MnO}_2@\text{Co}_3\text{O}_4$ CV curve at various current densities. **b** The b value curve produced by the interaction between peak current and scan rate. **c** Ratios of capacity contribution at various scan rates. **d**

EIS spectra of MnO_2 and $\text{MnO}_2@\text{Co}_3\text{O}_4$ after activation cycles. **e** GITT curves during charge/discharge procedures at a current density of 0.2 A g^{-1} and the related ion diffusion coefficient

$$i(v) = k_1 v + k_2 v^{1/2} \quad (3)$$

As shown in Fig. 5c, the capacitance contributions are 34.6%, 39.8%, 44.6%, 47.8%, 50.5%, and 62.0% at scan speeds of 0.2, 0.4, 0.6, 0.8, 1.0, and 2.0 mV s⁻¹, respectively. This demonstrates how, due to dynamics of fast charge transfer, capacitive behavior contributes more at high current densities. In general, the diffusion process still predominates, which may be caused by the intimate contact between Co₃O₄ nanocrystals and MnO₂ nanorods, generating heterogeneous structures and accomplishing the quick transfer of ions [32]. The fitted equivalent circuit design is used to illustrate the electrochemical impedance spectra of MnO₂ and MnO₂@Co₃O₄ electrodes as determined by EIS technology following activation cycles in Fig. 5d. The low-frequency regions indicate the ion diffusion rate at the electrode–electrolyte interface, while the high-frequency regions represent the charge transfer impedance of electrode materials [33]. The MnO₂@Co₃O₄ electrode has a semicircular radius that is somewhat bigger than that of the MnO₂ electrode before the cycle, which may be the result of insufficient electrolyte infiltration and contact, leading to significant charge transfer resistance (Fig. S4). After the initial cycle activation, the ion diffusion path in Fig. 5d lowers the resistance to charge transfer as a result of the electrolyte's complete penetration and the establishment of the electrolyte interface [34]. To further investigate the effect of Co₃O₄ nanocrystalline coating on kinetics, the ionic diffusion rate of the MnO₂@Co₃O₄ electrode was measured using the galvanostatic intermittent titration technique (GITT). From the amplified discharge process (Fig. S5), it passes through the pulse stage prior to the constant current stage, the constant discharge stage, and lastly the relaxation stage, during which the voltage increases to equilibrium. On the other side, the charging process involves the exact opposite approach (Fig. S6). To evaluate the effect of MnO₂@Co₃O₄ composite on diffusion kinetics, it is possible to compute the diffusion coefficient (D^{GITT}) using the following formula [35]:

$$D^{GITT} = \frac{4}{\pi \cdot \tau} \left(\frac{m_B V_M}{M_B S} \right)^2 \left(\frac{\Delta E_s}{\Delta E_t} \right)^2 \quad (4)$$

where the mass is represented by m_B (g), the molar volume by V_M (cm³ mol⁻¹), and the molar mass by M_B (g mol⁻¹). τ is constant current pulse period (s), S is the surface where the electrode and electrolyte make contact (cm²), ΔE_s is the voltage change resulting from a pulse (V), while ΔE_t is the voltage change resulting from charge and discharge with constant current (V). According to Fig. 5e and S7, MnO₂@Co₃O₄ had a calculated D^{GITT} value between 10⁻¹² and 10⁻¹⁰ cm² s⁻¹, which was greater than that of β -MnO₂ nanorods (range of 10⁻¹³ to 10⁻¹¹ cm² s⁻¹). Additionally, the two different discharge platforms also result in two distinct stages with respect to diffusion coefficients in the discharge process. Through

GITT calculations, we prove that the unique heterogeneous structure of MnO₂@Co₃O₄ electrode accelerates the ionic diffusion rate and shows excellent reaction kinetics. The construction of heterogeneous structure will provide a new idea for the study of manganese-based oxide cathode materials.

Conclusion

In conclusion, MnO₂@Co₃O₄ reversible aqueous ZIB cathode material has been prepared by PVP-assisted hydrothermal and calcination method. The synergistic effect of MnO₂@Co₃O₄ heterostructures enhances the ion diffusion kinetics and structural stability. MnO₂@Co₃O₄ composite has a greater specific capacity and improved rate performance compared to manganese dioxide electrode. In addition, the GITT test also confirms the claim that the nanocrystalline coating increased ion diffusion coefficient. High-performance aqueous zinc ion battery can greatly benefit from the heterostructure cathode, as demonstrated by the MnO₂@Co₃O₄ composite's remarkable electrochemical performance. This study provides a new, straightforward method for creating high-performance ZIB cathode materials.

Supplementary Information The online version contains supplementary material available at <https://doi.org/10.1007/s11581-023-04955-7>.

Funding The Fundamental Research Funds for the Central Universities (3132019328).

Data Availability The data that support the findings of this study are available from the corresponding author upon reasonable request.

References

1. Tarascon J-M, Armand M (2001) Issues and challenges facing rechargeable lithium batteries. *Nature* 414:359–367. <https://doi.org/10.1038/35104644>
2. Ge J, Fan L, Wang J et al (2018) MoSe₂/N-doped carbon as anodes for potassium-ion batteries. *Adv Energy Mater* 8:1801477. <https://doi.org/10.1002/aenm.201801477>
3. Li C, Shi X, Liang S et al (2020) Spatially homogeneous copper foam as surface dendrite-free host for zinc metal anode. *Chem Eng J* 379:122248. <https://doi.org/10.1016/j.cej.2019.122248>
4. Alfaruqi MH, Mathew V, Gim J et al (2015) Electrochemically induced structural transformation in a γ -MnO₂ cathode of a high capacity zinc-ion battery system. *Chem Mater* 27:3609–3620. <https://doi.org/10.1021/cm504717p>
5. Pan H, Shao Y, Yan P et al (2016) Reversible aqueous zinc/manganese oxide energy storage from conversion reactions. *Nat Energy* 1:16039. <https://doi.org/10.1038/nenergy.2016.39>
6. Ruan P, Xu X, Zheng D et al (2022) Promoting reversible dissolution/deposition of MnO₂ for high-energy-density zinc batteries via enhancing cut-off voltage. *ChemSusChem* 15:e202201118. <https://doi.org/10.1002/cssc.202201118>
7. Li C, Zhang X, He W et al (2020) Cathode materials for rechargeable zinc-ion batteries: From synthesis to mechanism and

- applications. *J Power Sources* 449:227596. <https://doi.org/10.1016/j.jpowsour.2019.227596>
8. Lee Y-G, Lee J, An G (2021) Free-standing manganese oxide on flexible graphene films as advanced electrodes for stable, high energy-density solid-state zinc-ion batteries. *Chem Eng J* 414:128916. <https://doi.org/10.1016/j.cej.2021.128916>
 9. Blanc LE, Kundu D, Nazar LF (2020) Scientific challenges for the implementation of Zn-Ion batteries. *Joule* 4:771–799. <https://doi.org/10.1016/j.joule.2020.03.002>
 10. Tang F, Wu X, Shen Y et al (2022) The intercalation cathode materials of heterostructure MnS/MnO with dual ions defect embedded in N-doped carbon fibers for aqueous zinc ion batteries. *Energy Storage Mater* 52:180–188. <https://doi.org/10.1016/j.ensm.2022.07.033>
 11. Zhou S, Wu X, Du H et al (2022) Dual metal ions and water molecular pre-intercalated δ -MnO₂ spherical microflowers for aqueous zinc ion batteries. *J Colloid Interface Sci* 623:456–466. <https://doi.org/10.1016/j.jcis.2022.05.018>
 12. Long F, Xiang Y, Yang S et al (2022) Layered manganese dioxide nanoflowers with Cu²⁺ and Bi³⁺ intercalation as high-performance cathode for aqueous zinc-ion battery. *J Colloid Interface Sci* 616:101–109. <https://doi.org/10.1016/j.jcis.2022.02.059>
 13. Wang Q, Sun J, Wang Q et al (2015) Electrochemical performance of α -MoO₃-In₂O₃ core-shell nanorods as anode materials for lithium-ion batteries. *J Mater Chem A* 3:5083–5091. <https://doi.org/10.1039/C5TA00127G>
 14. Li Y, Fu Y, Liu W et al (2019) Hollow Co-Co₃O₄@CNTs derived from ZIF-67 for lithium ion batteries. *J Alloy Compd* 784:439–446. <https://doi.org/10.1016/j.jallcom.2019.01.085>
 15. Huang G, Zhang F, Du X et al (2015) Metal organic frameworks route to *in situ* insertion of multiwalled carbon nanotubes in Co₃O₄ polyhedra as anode materials for lithium-ion batteries. *ACS Nano* 9:1592–1599. <https://doi.org/10.1021/nn506252u>
 16. Liang Y, Wu D, Feng X, Müllen K (2009) Dispersion of graphene sheets in organic solvent supported by ionic interactions. *Adv Mater* 21:1679–1683. <https://doi.org/10.1002/adma.200803160>
 17. Zhang J, Li F, Chen W et al (2019) Facile synthesis of hollow Co₃O₄-embedded carbon/reduced graphene oxides nanocomposites for use as efficient electrocatalysts in oxygen evolution reaction. *Electrochim Acta* 300:123–130. <https://doi.org/10.1016/j.electacta.2019.01.100>
 18. Huang S, Wang M, Jia P et al (2019) N-graphene motivated SnO₂@SnS₂ heterostructure quantum dots for high performance lithium/sodium storage. *Energy Storage Mater* 20:225–233. <https://doi.org/10.1016/j.ensm.2018.11.024>
 19. Liu H, Cao K, Li W et al (2019) Constructing hierarchical MnO₂/Co₃O₄ heterostructure hollow spheres for high-performance Li-Ion batteries. *J Power Sources* 437:226904. <https://doi.org/10.1016/j.jpowsour.2019.226904>
 20. Zhang N, Cheng F, Liu J et al (2017) Rechargeable aqueous zinc-manganese dioxide batteries with high energy and power densities. *Nat Commun* 8:405. <https://doi.org/10.1038/s41467-017-00467-x>
 21. Sun W, Wang F, Hou SY et al (2017) Zn/MnO₂ battery chemistry with H⁺ and Zn²⁺ coinserction. *J Am Chem Soc* 139:9775–9778. <https://doi.org/10.1021/jacs.7b04471>
 22. Liu M, Zhao Q, Liu H et al (2019) Tuning phase evolution of β -MnO₂ during microwave hydrothermal synthesis for high-performance aqueous Zn ion battery. *Nano Energy* 64:103942. <https://doi.org/10.1016/j.nanoen.2019.103942>
 23. Xu J-W, Gao Q-L, Xia Y-M et al (2021) High-performance reversible aqueous zinc-ion battery based on iron-doped alpha-manganese dioxide coated by polypyrrole. *J Colloid Interface Sci* 598:419–429. <https://doi.org/10.1016/j.jcis.2021.04.057>
 24. Alfaruqi MH, Gim J, Kim S et al (2015) Enhanced reversible divalent zinc storage in a structurally stable α -MnO₂ nanorod electrode. *J Power Sources* 288:320–327. <https://doi.org/10.1016/j.jpowsour.2015.04.140>
 25. Jiang W, Xu X, Liu Y et al (2020) Facile plasma treated β -MnO₂@C hybrids for durable cycling cathodes in aqueous Zn-ion batteries. *J Alloys Compd* 827:154273. <https://doi.org/10.1016/j.jallcom.2020.154273>
 26. Jiang B, Xu C, Wu C et al (2017) Manganese sesquioxide as cathode material for multivalent zinc ion battery with high capacity and long cycle life. *Electrochim Acta* 229:422–428. <https://doi.org/10.1016/j.electacta.2017.01.163>
 27. Alfaruqi MH, Gim J, Kim S et al (2015) A layered δ -MnO₂ nanoflake cathode with high zinc-storage capacities for eco-friendly battery applications. *Electrochem Commun* 60:121–125. <https://doi.org/10.1016/j.elecom.2015.08.019>
 28. Kim S, Koo B-R, Jo Y-R et al (2021) Defect engineering *via* the F-doping of β -MnO₂ cathode to design hierarchical spheres of intercalated nanosheets for superior high-rate aqueous zinc ion batteries. *J Mater Chem A* 9:17211–17222. <https://doi.org/10.1039/D1TA04051K>
 29. Lindström H, Södergren S, Solbrand A et al (1997) Li⁺ ion insertion in TiO₂ (Anatase). 2. voltammetry on nanoporous films. *J Phys Chem B* 101:7717–7722. <https://doi.org/10.1021/jp970490q>
 30. Wang J, Polleux J, Lim J, Dunn B (2007) Pseudocapacitive contributions to electrochemical energy storage in TiO₂ (anatase) nanoparticles. *J Phys Chem C* 111:14925–14931. <https://doi.org/10.1021/jp074464w>
 31. Brezesinski T, Wang J, Polleux J et al (2009) Templated nanocrystal-based porous TiO₂ films for next-generation electrochemical capacitors. *J Am Chem Soc* 131:1802–1809. <https://doi.org/10.1021/ja8057309>
 32. Wang H, Zheng Y, Peng Z et al (2021) Nanocavity-enriched Co₃O₄@ZnCo₂O₄@NC porous nanowires derived from 1D metal coordination polymers for fast Li⁺ diffusion kinetics and super Li⁺ storage. *Dalton Trans* 50:7277–7283. <https://doi.org/10.1039/D1DT00475A>
 33. Niu C, Meng J, Wang X et al (2015) General synthesis of complex nanotubes by gradient electrospinning and controlled pyrolysis. *Nat Commun* 6:7402. <https://doi.org/10.1038/ncomms8402>
 34. Xu J, Wang M, Wickramaratne NP et al (2015) High-performance sodium ion batteries based on a 3D anode from nitrogen-doped graphene foams. *Adv Mater* 27:2042–2048. <https://doi.org/10.1002/adma.201405370>
 35. Deiss E (2005) Spurious chemical diffusion coefficients of Li⁺ in electrode materials evaluated with GITT. *Electrochim Acta* 50:2927–2932. <https://doi.org/10.1016/j.electacta.2004.11.042>

Publisher's note Springer Nature remains neutral with regard to jurisdictional claims in published maps and institutional affiliations.

Springer Nature or its licensor (e.g. a society or other partner) holds exclusive rights to this article under a publishing agreement with the author(s) or other rightsholder(s); author self-archiving of the accepted manuscript version of this article is solely governed by the terms of such publishing agreement and applicable law.